AAS 24-318

COMPARATIVE ANALYSIS OF ANALYTICAL AND DATA-DRIVEN KOOPMAN OPERATORS FOR THE J2 PROBLEM WITH ATMOSPHERIC DRAG

Christian Hofmann,* Giovanni Lavezzi,† Di Wu,‡ Simone Servadio,§ Richard Linares¶

We advance the application of the Koopman operator theory (KOT), a method to transform a nonlinear dynamical system into a linear one, for the perturbed motion of a satellite around a central body. Our approach introduces a novel numerical technique utilizing quadrature points for training data and employing differentiated weighting of training samples compared to the state-of-the-art Extended Dynamic Mode Decomposition method. Additionally, KOT is extended to encompass the motion of a satellite subject to atmospheric drag, enabling the analytical prediction of future states. We further assess the propagation accuracy for analytical and data-driven methods.

INTRODUCTION

Dynamical systems governing space objects are inherently nonlinear, lacking a comprehensive framework for their general description. Linear systems benefit from spectral decomposition, allowing efficient algorithms for prediction and control.[1] Nonlinear models, however, often rely on algorithms and theorems designed for linear systems, making it challenging to achieve model fidelity and extract insights. Even though linearizing dynamics around a reference point is common, accuracy is lost with distance from the reference. Depending on the application, such a local approximation may not be appropriate.

Koopman operator theory (KOT) offers a global approach by transforming nonlinear systems into a higher-dimensional space for a linear representation.[2] This theory globally describes the evolution of observable functions. However, managing the infinite-dimensional space is challenging, necessitating truncation in real-world applications. Data-driven techniques like Dynamic Mode Decomposition (DMD) and Extended Dynamic Mode Decomposition (EDMD) help approximate the Koopman operator in finite dimensions, optimizing model fidelity using available data. These methods have been applied in fields like engineering[3] and robotics,[4] demonstrating their utility. Despite

*Postdoctoral Associate, Department of Aeronautics and Astronautics, Massachusetts Institute of Technology, Cambridge, MA 02139, USA. Email: hofmannc@mit.edu

†Postdoctoral Associate, Department of Aeronautics and Astronautics, Massachusetts Institute of Technology, Cambridge, MA 02139, USA. Email: glavezzi@mit.edu

‡Postdoctoral Associate, Department of Aeronautics and Astronautics, Massachusetts Institute of Technology, Cambridge, MA 02139, USA. Email: d_wu@mit.edu@mit.edu

§Assistant Professor, Department of Aerospace Engineering, Iowa State University, Ames, IA 50011, USA. Email: servadio@iastate.edu

¶Associate Professor, Department of Aeronautics and Astronautics, Massachusetts Institute of Technology, Cambridge, MA 02139, USA. Email: linaresr@mit.edu

its potential, KOT's application in astrodynamics is limited due to stringent accuracy requirements. Recent advancements in analytical KOT have addressed challenges such as the zonal harmonics problem[5] attitude dynamics,[6] and uncertainty propagation.[7]

Data-driven methodologies have also found applications in space engineering, for example to determine control laws for the circular-restricted three-body problem (CRTBP),[8,9] and recent studies make use of direct encoding approach[10] and neural networks.[11] Most data-driven methods rely on random sampling for training data due to its simplicity, but capturing complex nonlinearities often requires more sophisticated data generation. Recent research focuses on theoretical insights when EDMD is applied to stochastic systems and alternative sampling methods are used.[12] Additionally, a novel method for computing spectra and pseudospectra of Koopman operators using snapshot data has been introduced, successfully applied to examples like the pendulum with Legendre-Gauss sampling. Still, the efficient inclusion of large datasets and comparison of different sampling methods for astrodynamics problems remain areas for further research.

In this work, we propose the use of sparse grid quadrature points to generate the training data for EDMD. This way, the computational effort and number of samples can be reduced. Moreover, we consider atmospheric drag in the Koopman operator theory, and compare the performance of an analytical and data-driven approach.

The paper is structured as follows. The following section addresses Koopman operator theory, EDMD, and sparse grid quadrature EDMD. Next, the J_2 and atmospheric drag problem are formulated. Finally, numerical simulations are performed, followed by conclusive remarks.

KOOPMAN OPERATOR THEORY AND EXTENDED DYNAMIC MODE DECOMPOSITION

Given a dynamical system with dynamics $\mathbf{f}(\mathbf{x}(t))$ and states $\mathbf{x} \in \mathbb{R}^n$

$$\frac{\mathrm{d}}{\mathrm{d}t}\mathbf{x}(t) = \mathbf{f}(\mathbf{x}(t)) \tag{1}$$

the Koopman operator describes the evolution of observable functions in an infinite-dimensional space. The operator is often projected onto basis functions $\mathbf{L}(\mathbf{x}) = [L_1(\mathbf{x}), L_2(\mathbf{x}), \ldots, L_m(\mathbf{x})]$ using the Galerkin method to obtain

$$\frac{\mathrm{d}}{\mathrm{d}t}\mathbf{L}(\mathbf{x}) = \mathbf{K}\,\mathbf{L}(\mathbf{x}) \tag{2}$$

$\mathbf{K}$ is a finite-dimensional Koopman matrix that approximates the Koopman operator. Its elements K_{ij} are given by:[5]

$$K_{ij} = \langle (\nabla_{\mathbf{x}} L_i(\mathbf{x}))\ \mathbf{f}(\mathbf{x}), L_j(\mathbf{x}) \rangle \tag{3}$$

where $\langle \cdot, \cdot \rangle$ is the inner product, and L_i, $i = 1, \ldots, m$, and L_j, $j = 1, \ldots, m$, denote the basis functions. The inner product is given by

$$\langle (\nabla_{\mathbf{x}} L_i(\mathbf{x}))\ \mathbf{f}(\mathbf{x}), L_j(\mathbf{x}) \rangle = \int_{\Omega} (\nabla_{\mathbf{x}} L_i(\mathbf{x}))\ \mathbf{f}(\mathbf{x})\, L_j(\mathbf{x})\, w(\mathbf{x})\, \mathrm{d}\mathbf{x} \tag{4}$$

In this work, we use Legendre polynomials with weighting function $w(\mathbf{x}) \equiv 1$ and domain $\Omega = [-1, 1]^n$. After performing an eigendecomposition of $\mathbf{K}$ to obtain a matrix $\mathbf{V}_r$ of the right eigenvectors and the diagonal matrix $\mathbf{D}$ of eigenvalues, future states at time t can be computed analytically:[13]

$$\mathbf{x}(t) = \mathbf{G}\,\mathbf{V}_r\,\mathrm{e}^{\mathbf{D}\,t}\,\mathbf{V}_r^{-1}\,\mathbf{L}(\mathbf{x}_0) \tag{5}$$

where $\mathbf{G}$ is a constant transformation matrix that projects the states onto the basis functions and satisfies

$$\mathbf{x} = \mathbf{G}\,\mathbf{L}(\mathbf{x}) \tag{6}$$

Its elements are given by $G_{ij} = \langle x_i, L_j \rangle$. $\mathbf{x}_0$ denotes the initial condition.

Instead of using the Galerkin method to obtain a finite-dimensional approximation of the Koopman matrix, data-driven methods like Extended Dynamic Mode Decomposition (EDMD) can be used to approximate $\mathbf{K}$. Given the training data $\mathbf{X} = [\mathbf{x}_1\ \mathbf{x}_2\ \ldots\ \mathbf{x}_M]$ and $\mathbf{Y} = [\mathbf{y}_1\ \mathbf{y}_2\ \ldots\ \mathbf{y}_M]$, where $\mathbf{x}_i$ denotes the ith snapshot of the state of the system, and $\mathbf{y}_i$ the corresponding state when solving Eq. (1), a least-squares problem is solved to obtain the discrete-time Koopman matrix $\tilde{\mathbf{K}}$ from data:[14]

$$\min_{\tilde{\mathbf{K}} \in \mathbb{R}^{\eta \times \eta}} \sum_{i=1}^{M} \left\| \mathbf{L}(\mathbf{y}_i) - \tilde{\mathbf{K}}\,\mathbf{L}(\mathbf{x}_i) \right\|_F^2 \tag{7}$$

where $\mathbf{L}(\mathbf{x}) = [L_1(\mathbf{x}), L_2(\mathbf{x}), \ldots, L_m(\mathbf{x})]$ are again the basis functions. The Koopman matrix is then given by

$$\tilde{\mathbf{K}} = \left(\mathbf{Q}^\top \mathbf{Q}\right)^{-1} \mathbf{Q}^\top \mathbf{P} \tag{8}$$

with

$$\mathbf{Q} = \frac{1}{M} \sum_{m=1}^{M} \mathbf{L}(\mathbf{x}_m)^\top \mathbf{L}(\mathbf{x}_m), \tag{9}$$

$$\mathbf{P} = \frac{1}{M} \sum_{m=1}^{M} \mathbf{L}(\mathbf{x}_m)^\top \mathbf{L}(\mathbf{y}_m) \tag{10}$$

The discrete Koopman matrix $\tilde{\mathbf{K}}$ is based on a specific time step Δt that was used for the training. Making use of

$$\tilde{\mathbf{K}} = \mathbf{V}_r\, \mathrm{e}^{\mathbf{D}\,\Delta t}\, \mathbf{V}_r^{-1} \tag{11}$$

and the matrix exponential, we obtain the following relationship between the discrete- and continuous-time Koopman matrices:

$$\log \tilde{\mathbf{K}} = \log\left(\mathrm{e}^{\mathbf{V}_r\,\mathbf{D}\,\Delta t\,\mathbf{V}_r^{-1}}\right) = \mathbf{V}_r\,\mathbf{D}\,\Delta t\,\mathbf{V}_r^{-1} = \mathbf{K}\,\Delta t \tag{12}$$

Quadrature-Based EDMD

Usually, the training data is randomly sampled for EDMD, and each point is weighted equally in Eqs. (9) and (10). In this work, we propose an extension of this traditional method by using quadrature nodes for the training data, therefore referred to as qEDMD. Therefore, the set $\mathbf{X} = [\mathbf{x}_1\ \mathbf{x}_2\ \ldots\ \mathbf{x}_M]$ is now comprised of quadrature nodes, and the corresponding weights w are included in the computation of $\mathbf{Q}$ and $\mathbf{P}$:[12]

$$\mathbf{Q} = \sum_{m=1}^{M} w_m^q \mathbf{L}(\mathbf{x}_m^q)^T \mathbf{L}(\mathbf{x}_m^q) \tag{13}$$

$$\mathbf{P} = \sum_{m=1}^{M} w_m^q \mathbf{L}(\mathbf{x}_m^q)^T \mathbf{L}(\mathbf{y}_m^q) \tag{14}$$

As the number of dimensions increases, the product rule faces the curse of dimensionality, with node counts in a full tensor grid growing exponentially, represented by N^k for dimension k. In this work, we consider a maximum dimension of $k = 8$, leading to an impractically large number of nodes for higher orders. To mitigate this issue, we use sparse grid quadrature, which selects a subset of points in the multidimensional space, significantly reducing the number of nodes needed. Specifically, we employ the Smolyak rule to create the sparse grid, using univariate nested Kronrod-Patterson rules as the basis. We opt for a nested rule since it demands fewer points for higher-dimensional problems. Furthermore, the Kronrod-Patterson rule has highly efficient implementations available.[15]

Separate Computation of Koopman Matrices

To compute a finite-dimensional approximation of the Koopman matrix using the Galerkin method, it is necessary to evaluate the integrals in Eq. (3). For polynomial systems, this can be done analytically. For non-polynomial systems, the qEDMD approach can be used to obtain $\mathbf{K}$. Therefore, the choice between Galerkin and qEDMD depends on the nature of the system being analyzed. In orbital motion problems, the accuracy of the dynamical model can be enhanced by incorporating additional perturbations. Here, the dynamics $\mathbf{f}(\mathbf{x})$ are expressed as the sum of the natural motion $\mathbf{f}_0(\mathbf{x})$ and perturbing terms $\mathbf{f}_i(\mathbf{x})$, where $i = 1, \ldots, n$ and n is the number of perturbations considered:

$$\mathbf{f}(\mathbf{x}) = \mathbf{f}_0(\mathbf{x}) + \mathbf{f}_1(\mathbf{x}) + \cdots + \mathbf{f}_n(\mathbf{x}) \tag{15}$$

This allows for the separate computation of Koopman matrices for each perturbation using Eq. (3), which can then be summed to obtain $\mathbf{K}$ for the complete system:

$$\begin{aligned} K_{ij} &= \underbrace{\int_\Omega [\nabla_\mathbf{x} L_i(\mathbf{x})]\ \mathbf{f}_0(\mathbf{x})\, L_j(\mathbf{x})\,\mathrm{d}\mathbf{x}}_{=:K_{0,ij}} + \cdots + \underbrace{\int_\Omega [\nabla_\mathbf{x} L_i(\mathbf{x})]\ \mathbf{f}_n(\mathbf{x})\, L_j(\mathbf{x})\,\mathrm{d}\mathbf{x}}_{=:K_{n,ij}} \\ &= K_{0,ij} + \cdots + K_{n,ij} \end{aligned} \tag{16}$$

For example, if part of the dynamics is polynomial and another part is not, it is advantageous to compute the polynomial system using the Galerkin method for higher accuracy and lower computational effort. The non-polynomial component can be handled using qEDMD. The overall Koopman matrix for the system is then the sum of the matrices computed for each component.

PERTURBED KEPLERIAN MOTION

We consider the perturbed Keplerian motion for the simulations. In particular, we consider the J_2 perturbation and atmospheric drag in the Koopman operator theory.

J2 Perturbation

We use a set of orbital elements that has proven to perform well for the Koopman approach.[5] The states $\mathbf{x} = [\Lambda, \eta, \gamma, s, \kappa, \beta, \chi, \rho]^\top$, can be derived from spherical coordinates, and the equations of motion read:[16]

$$\frac{\mathrm{d}\Lambda}{\mathrm{d}\tau} = -\eta + 3\, J_2\, s\, \gamma\, \kappa^3\, (2\,\kappa + \Lambda)\, (\kappa + \Lambda) \tag{17a}$$

$$\frac{\mathrm{d}\eta}{\mathrm{d}\tau} = \Lambda + \frac{3}{2}\, J_2\, \kappa^3\, (3\, s^2 - 1)\, (\kappa + \Lambda) \tag{17b}$$

$$\frac{\mathrm{d}\gamma}{\mathrm{d}\tau} = -s - 3\,J_2\,s\,\rho^2\,\kappa^3\,(\kappa+\Lambda) \tag{17c}$$

$$\frac{\mathrm{d}s}{\mathrm{d}\tau} = \gamma \tag{17d}$$

$$\frac{\mathrm{d}\kappa}{\mathrm{d}\tau} = 3\,J_2\,s\,\gamma\,\kappa^4\,(\kappa+\Lambda) \tag{17e}$$

$$\frac{\mathrm{d}\beta}{\mathrm{d}\tau} = -3\,J_2\,s^2\,\chi\,(\kappa+\Lambda) \tag{17f}$$

$$\frac{\mathrm{d}\chi}{\mathrm{d}\tau} = 6\,J_2\,s\,\gamma\,\chi\,(\kappa+\Lambda)\,(2\,\kappa^3+\rho\,\chi) \tag{17g}$$

$$\frac{\mathrm{d}\rho}{\mathrm{d}\tau} = 3\,J_2\,s\,\gamma\,\rho\,\kappa^3\,(\kappa+\Lambda) \tag{17h}$$

where a time regularization was performed:

$$\frac{\mathrm{d}\tau}{\mathrm{d}t} = \frac{p_\theta}{r^2} \tag{18}$$

with $p_\theta = \sqrt{p_\phi^2 + p_\theta^2/\cos^2\phi}$ being the angular momentum. Note that we added a γ in the differential equation of χ in Eq. (17g) that is erroneously missing in previous works.[5,16] The relationship to spherical coordinates is given by

$$\Lambda = \left(\frac{p_\theta}{r} - \frac{\mu}{p_\theta}\right)\sqrt{\frac{C}{\mu}} \tag{19}$$

$$\eta = p_r\sqrt{\frac{C}{\mu}} \tag{20}$$

$$s = \sin\phi \tag{21}$$

$$\gamma = \frac{p_\phi}{p_\theta}\cos\phi \tag{22}$$

$$\kappa = \frac{1}{p_\theta}\sqrt{C\,\mu} \tag{23}$$

$$\beta = \lambda - \arcsin\left(\tan\phi\sqrt{\frac{p_\lambda^2}{p_\theta^2 - p_\lambda^2}}\right) \tag{24}$$

$$\chi = \frac{p_\lambda}{p_\theta^2}\,\frac{(C\,\mu)^{3/2}}{p_\theta^2\,\sin^2\phi + p_\phi^2\,\cos^2\phi} \tag{25}$$

$$\rho = \frac{p_\lambda}{p_\theta} \tag{26}$$

C is a scaling factor and μ the gravitational parameter. The radial distance is denoted by r, the polar angle by ϕ, and the azimuthal angle by λ. The corresponding conjugate momenta are p_r, p_ϕ, and p_λ, respectively:

$$p_r = \dot{r} \tag{27}$$

$$p_\lambda = r^2\,\dot{\lambda}\,\cos^2\phi \tag{28}$$

$$p_\phi = r^2\,\dot{\phi} \tag{29}$$

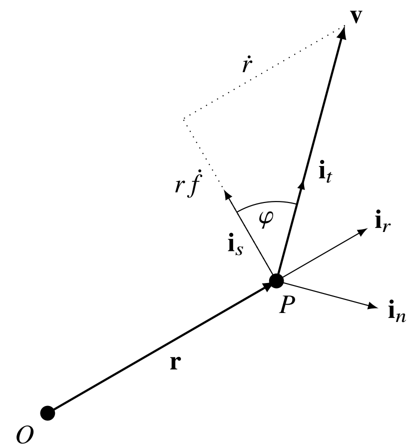

Figure 1: Coordinate frames RSW and NTW.

Atmospheric Drag

When a perturbing acceleration is added, the equations of motion for $[\Lambda, \eta, \gamma, s, \kappa, \beta]^\top$ read:[13]

$$\frac{\mathrm{d}\Lambda}{\mathrm{d}\tau} = -\eta + \frac{2\,\kappa + \Lambda}{\kappa\,(\kappa+\Lambda)^3}\,\frac{C^2}{\mu}\,a_s \tag{30a}$$

$$\frac{\mathrm{d}\eta}{\mathrm{d}\tau} = \Lambda + \frac{1}{\kappa\,(\kappa+\Lambda)^2}\,\frac{C^2}{\mu}\,a_r \tag{30b}$$

$$\frac{\mathrm{d}\gamma}{\mathrm{d}\tau} = -s + \frac{\sqrt{1-s^2-\gamma^2}}{\kappa\,(\kappa+\Lambda)^3}\,\frac{C^2}{\mu}\,a_w \tag{30c}$$

$$\frac{\mathrm{d}s}{\mathrm{d}\tau} = \gamma \tag{30d}$$

$$\frac{\mathrm{d}\kappa}{\mathrm{d}\tau} = -\frac{1}{(\kappa+\Lambda)^3}\,\frac{C^2}{\mu}\,a_s \tag{30e}$$

$$\frac{\mathrm{d}\beta}{\mathrm{d}\tau} = \frac{s}{(s^2+\gamma^2)\,\kappa\,(\kappa+\Lambda)^3}\,\frac{C^2}{\mu}\,a_w \tag{30f}$$

where the perturbing acceleration $\mathbf{a}_p$ is defined as:

$$\mathbf{a}_p = a_r\,\mathbf{i}_r + a_s\,\mathbf{i}_s + a_w\,\mathbf{i}_w \tag{31}$$

The unit vectors $\mathbf{i}_r$, $\mathbf{i}_s$, and $\mathbf{i}_w$ refer to the standard orbital frame RSW where the first axis points in the direction of the position vector, the third axis is along the orbit normal vector, and the second axis completes the coordinate system (see Fig. 1). The remaining equations of motion for χ and ρ can be derived in a similar fashion:

$$\frac{\mathrm{d}\chi}{\mathrm{d}\tau} = -\frac{3\,\kappa^2\,\sqrt{1-s^2-\gamma^2}}{(s^2+\gamma^2)^2\,(\kappa+\Lambda)^3}\,\frac{C^2}{\mu}\,a_s - \frac{\kappa^2\,\gamma\,(2-s^2-\gamma^2)}{(s^2+\gamma^2)^2\,(\kappa+\Lambda)^3}\,\frac{C^2}{\mu}\,a_w \tag{32a}$$

$$\frac{\mathrm{d}\rho}{\mathrm{d}\tau} = -\frac{\gamma}{\kappa\,(\kappa+\Lambda)^3}\,\frac{C^2}{\mu}\,a_w \tag{32b}$$

The perturbing acceleration $\mathbf{a}_d$ due to drag is

$$\mathbf{a}_d = -\frac{1}{2}\,\psi(h)\,v_{\mathrm{rel}}^2\,\frac{C_D\,A}{m}\,\mathbf{i}_t \tag{33}$$

where $\psi(h)$ is the atmospheric density that depends on the altitude h and is computed using the U.S. Standard Atmosphere 1976 (USSA76) model, A denotes the projected area of the spacecraft, C_D is the dimensionless drag coefficient, and m the mass of the spacecraft. The unit vector $\mathbf{i}_t$ points along the velocity vector. In this work, we neglect the velocity of the atmosphere and approximate the relative velocity $\mathbf{v}_{\mathrm{rel}}$ as the velocity of the spacecraft $\mathbf{v}$:

$$\mathbf{v}_{\mathrm{rel}} \approx \mathbf{v} \tag{34}$$

Dividing the velocity into radial and transversal components, we find the following relationship using Fig. 1:

$$v^2 = \dot{r}^2 + \left(r\,\dot{f}\right)^2 = p_r^2 + \frac{p_\theta^2}{r^2} \tag{35}$$

where f is the true anomaly and $\dot{f} = p_\theta/r^2$. The radius r is

$$r = \frac{C}{\kappa^2 + \kappa\,\Lambda} \tag{36}$$

and the magnitude of the relative velocity can then be expressed as

$$v_{\mathrm{rel}}^2 = v^2 = \frac{\mu}{C}\,\left[\eta^2 + (\kappa + \Lambda)^2\right] \tag{37}$$

Making use of the flight path angle φ and Fig. 1, we obtain a relationship between the RSW and NTW frame where the second axis $\mathbf{i}_t$ points along the velocity vector, the third axis $\mathbf{i}_w$ points along the orbit normal, and the first axis $\mathbf{i}_n$ completes the coordinate frame:

$$\begin{pmatrix}\mathbf{i}_r\\ \mathbf{i}_s\end{pmatrix} = \begin{pmatrix}\cos\varphi & \sin\varphi\\ -\sin\varphi & \cos\varphi\end{pmatrix}\begin{pmatrix}\mathbf{i}_n\\ \mathbf{i}_t\end{pmatrix} \tag{38}$$

Comparing coefficients yields

$$a_r = a_n\,\cos\varphi + a_t\,\sin\varphi \tag{39}$$

$$a_s = -a_n\,\sin\varphi + a_t\,\cos\varphi \tag{40}$$

Drag can then be written in the NTW frame as

$$a_n = 0 \tag{41a}$$

$$a_t = -\frac{1}{2}\,\psi(h)\,v_{\mathrm{rel}}^2\,\frac{C_D\,A}{m} \tag{41b}$$

$$a_w = 0 \tag{41c}$$

Using $v = \sqrt{2\mu/r - \mu/a}$ and $a = -C/(\eta^2 - \kappa^2 + \Lambda^2)$, we obtain the following expressions from Fig. 1:

$$\cos\varphi = \frac{r\,\dot{f}}{v} = \frac{\kappa + \Lambda}{\sqrt{\eta^2 + (\kappa + \Lambda)^2}} \tag{42}$$

$$\sin\varphi = \frac{\dot{r}}{v} = \frac{\eta}{\sqrt{\eta^2 + (\kappa + \Lambda)^2}} \tag{43}$$

The equations of motion in the NTW frame are then given by:

$$\frac{\mathrm{d}\Lambda}{\mathrm{d}\tau} = -\eta - 0.5\,B\,\psi(h)\,C\,(2\,\kappa + \Lambda)\,\frac{\sqrt{\eta^2 + (\kappa+\Lambda)^2}}{\kappa\,(\kappa+\Lambda)^2} \tag{44a}$$

$$\frac{\mathrm{d}\eta}{\mathrm{d}\tau} = \Lambda - 0.5\,B\,\psi(h)\,C\,\eta\,\frac{\sqrt{\eta^2 + (\kappa+\Lambda)^2}}{\kappa\,(\kappa+\Lambda)^2} \tag{44b}$$

$$\frac{\mathrm{d}\gamma}{\mathrm{d}\tau} = -s \tag{44c}$$

$$\frac{\mathrm{d}s}{\mathrm{d}\tau} = \gamma \tag{44d}$$

$$\frac{\mathrm{d}\kappa}{\mathrm{d}\tau} = 0.5\,B\,\psi(h)\,C\,\eta\,\frac{\sqrt{\eta^2 + (\kappa+\Lambda)^2}}{(\kappa+\Lambda)^2} \tag{44e}$$

$$\frac{\mathrm{d}\beta}{\mathrm{d}\tau} = 0 \tag{44f}$$

$$\frac{\mathrm{d}\chi}{\mathrm{d}\tau} = 1.5\,B\,\psi(h)\,\frac{\chi}{\kappa}\,\frac{\sqrt{\eta^2 + (\kappa+\Lambda)^2}}{(\kappa+\Lambda)^2} \tag{44g}$$

$$\frac{\mathrm{d}\rho}{\mathrm{d}\tau} = 0 \tag{44h}$$

The ballistic coefficient and the altitude h are defined as follows:

$$B = \frac{C_D\,A}{m} \tag{45}$$

$$h = \frac{C}{\kappa^2 + \kappa\,\Lambda} - R_e \tag{46}$$

where R_e is the radius of the Earth. While the singularities in the denominators of Eqs. (44a), (44b), (44e), (44g) and (46) are not physically relevant as they would result in infeasible orbits, they pose a challenge when generating training data. Atmospheric drag affects only low-Earth orbits with altitudes up to about $2000\,\mathrm{km}$. To avoid singularities at $\kappa\,(\kappa+\Lambda)^2 = 0$ or negative altitudes, we propose shifting the quadrature points' domain for the relevant elements Λ, η, and κ. Specifically, for altitudes between $200\,\mathrm{km}$ to $2000\,\mathrm{km}$, the corresponding ranges are $\Lambda \in [-0.10, 0.09]$, $\eta \in [-0.15, 0.15]$, and $\kappa \in [0.87, 0.94]$. We perform a linear transformation for each element from the interval $[-1, 1]$ to these respective ranges.

NUMERICAL SIMULATIONS

We compare the accuracy of analytical propagation methods based on KOT (Galerkin, EDMD, and qEDMD) for the J_2 perturbation, atmospheric drag, and their combination. All methods use normalized Legendre polynomials as basis functions, with EDMD generating random training points within $[-1, 1]$ and qEDMD employing the Smolyak rule with Kronrod-Patterson basis rules to generate a sparse grid.[15] The number of training points for each method and quadrature order is detailed in Tables 1.

Accuracy is assessed by propagating 1000 randomly sampled initial conditions, representing low Earth, medium Earth, and geostationary orbits for J_2, and low Earth orbits for atmospheric drag. We report medians of the maximum position errors for each propagation. Simulation parameters are given in Table 2.

Table 1: Number of points and quadrature order for the J_2 and drag problem (eight states).

Number of points	Quadrature order
6657	6
17921	7
43137	8
97153	9
206465	10
411265	11

Table 2: Parameters for the simulations.

Parameter	Value
Gravitational parameter μ, $\mathrm{km}^3/\mathrm{s}^2$	$398\,600.4418$
Radius of Earth R_e, km	6378.137
Zonal coefficient J_2	0.0010826267
Spacecraft mass m, kg	100
Spacecraft area A, m^2	1
Drag coefficient C_D	2.2

J_2 Perturbation

For the J_2 problem, we propagate for 20 orbital revolutions, and Fig. 2 shows the median position error for EDMD and qEDMD with varying training points, compared to the Galerkin method. Both EDMD and qEDMD converge to the Galerkin solution with more training points, but qEDMD converges faster with fewer data points when using 5th order basis functions (see Fig. 2a). However, for higher-order basis functions (e.g., 7th order), qEDMD requires more points than EDMD to achieve similar accuracy, as shown in Fig. 2b. The corresponding plots to illustrate the influence of the quadrature order for qEDMD are shown in Figs. 3a and 3b.

Figure 4 compares different orders of basis functions for qEDMD. As expected, higher-order functions improve accuracy, with 7th order basis functions reducing the error significantly. However, increasing the number of grid points has a minor impact on lower-order basis functions' accuracy.

The eigenvalues of the Koopman matrix for 5th order basis functions (see Fig. 5) show that qEDMD matches the Galerkin method closely, while EDMD often deviates. This indicates qEDMD's superior accuracy, particularly with lower-order basis functions.

Atmospheric Drag

We also propagate for 20 revolutions when considering atmoshperic drag only. Figure 6 compares position error for EDMD and qEDMD. Initial conditions are chosen for low Earth orbits with periapsis radii between 200 and $1000\,\mathrm{km}$, and eccentricities between 0.0 and 0.1. qEDMD shows slightly higher accuracy, maintaining errors below $10\,\mathrm{km}$. However, EDMD exhibits large errors with 6657 grid points for 5th and 6th order basis functions, indicating insufficient random points

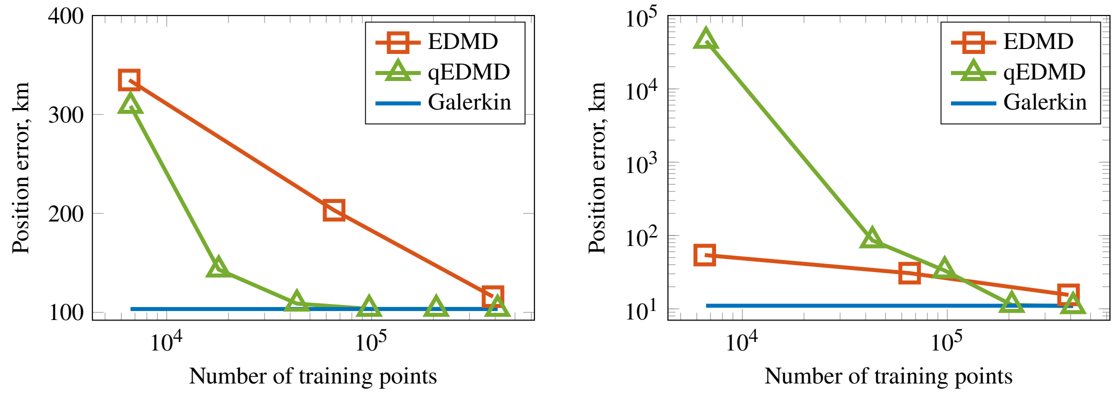

(a) 5th order basis functions.

(b) 7th order basis functions.

Figure 2: Comparison of position error for standard EDMD, qEDMD, and Galerkin for the propagation of a spacecraft under J_2 perturbation.

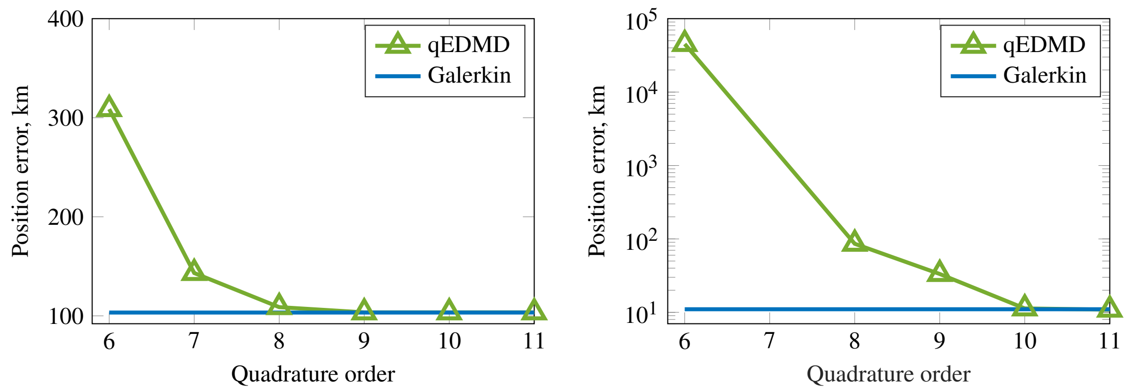

(a) 5th order basis functions.

(b) 7th order basis functions.

Figure 3: Comparison of position error for different qEDMD quadrature orders for the propagation of a spacecraft under J_2 perturbation.

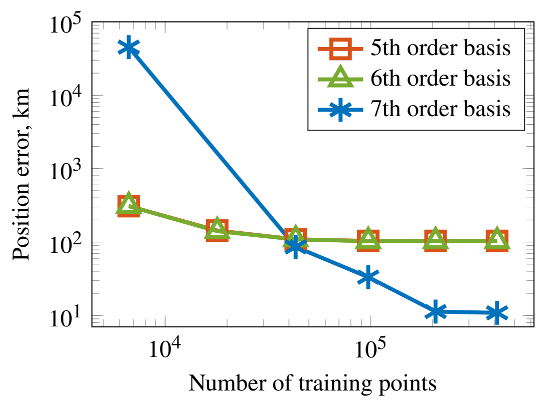

Figure 4: Comparison of position error for different basis function and qEDMD quadrature orders for the propagation of a spacecraft under J_2 perturbation

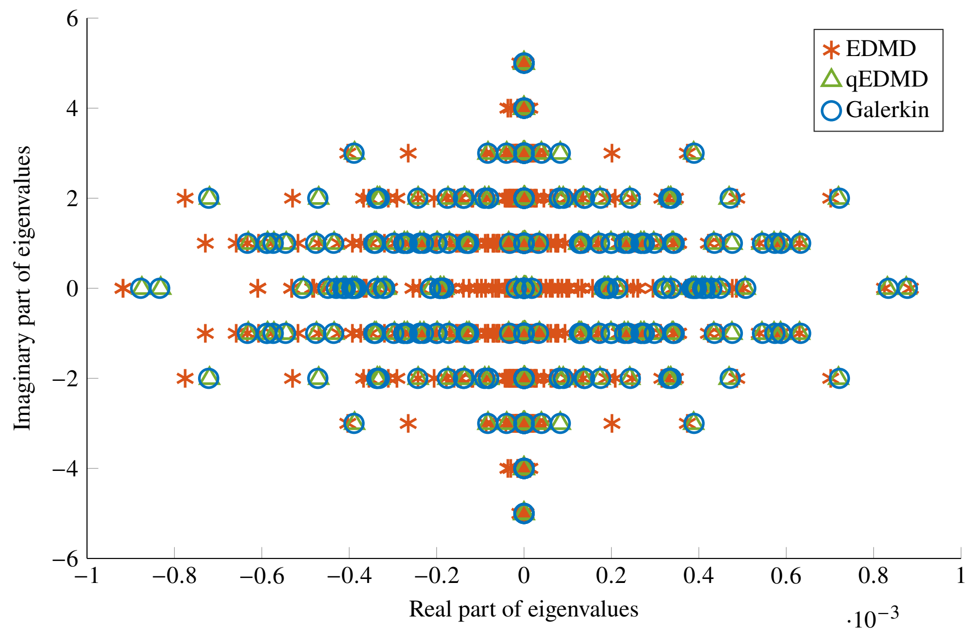

Figure 5: Comparison of eigenvalues for standard EDMD, qEDMD, and Galerkin for 5th order basis functions.

for accurate state prediction with drag. qEDMD achieves an error of less than $1\ \mathrm{km}$ with 5th order basis functions and 6657 grid points but requires higher quadrature orders for more accurate results with higher-order basis functions. Notably, for qEDMD with 5th order basis functions, the error increases slightly when the number of training points grows from 6657 to 43137 (see Fig. 6a). This likely results from changes in the conditioning of the Koopman matrix. For basis functions of order higher than 6, the matrix becomes ill-conditioned, leading to decreased accuracy.

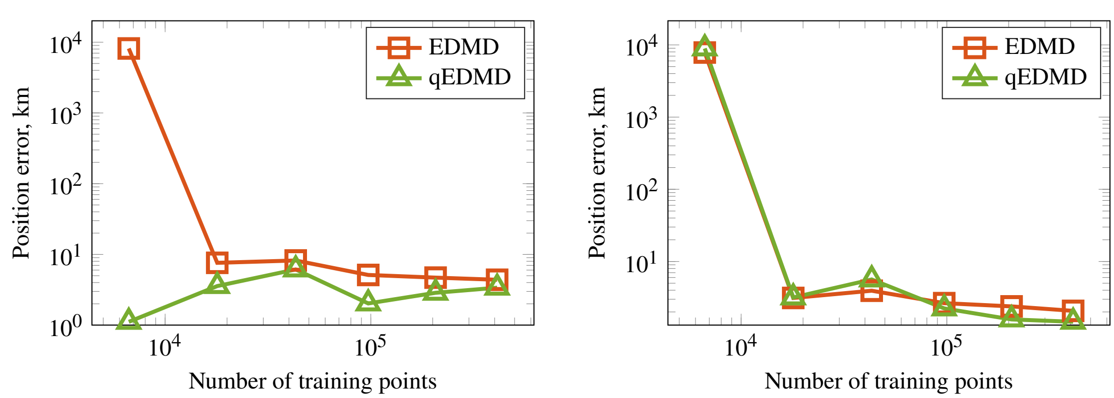

(a) 5th order basis functions.

(b) 6th order basis functions.

Figure 6: Comparison of position error for standard EDMD and qEDMD for the propagation of a spacecraft under atmospheric drag.

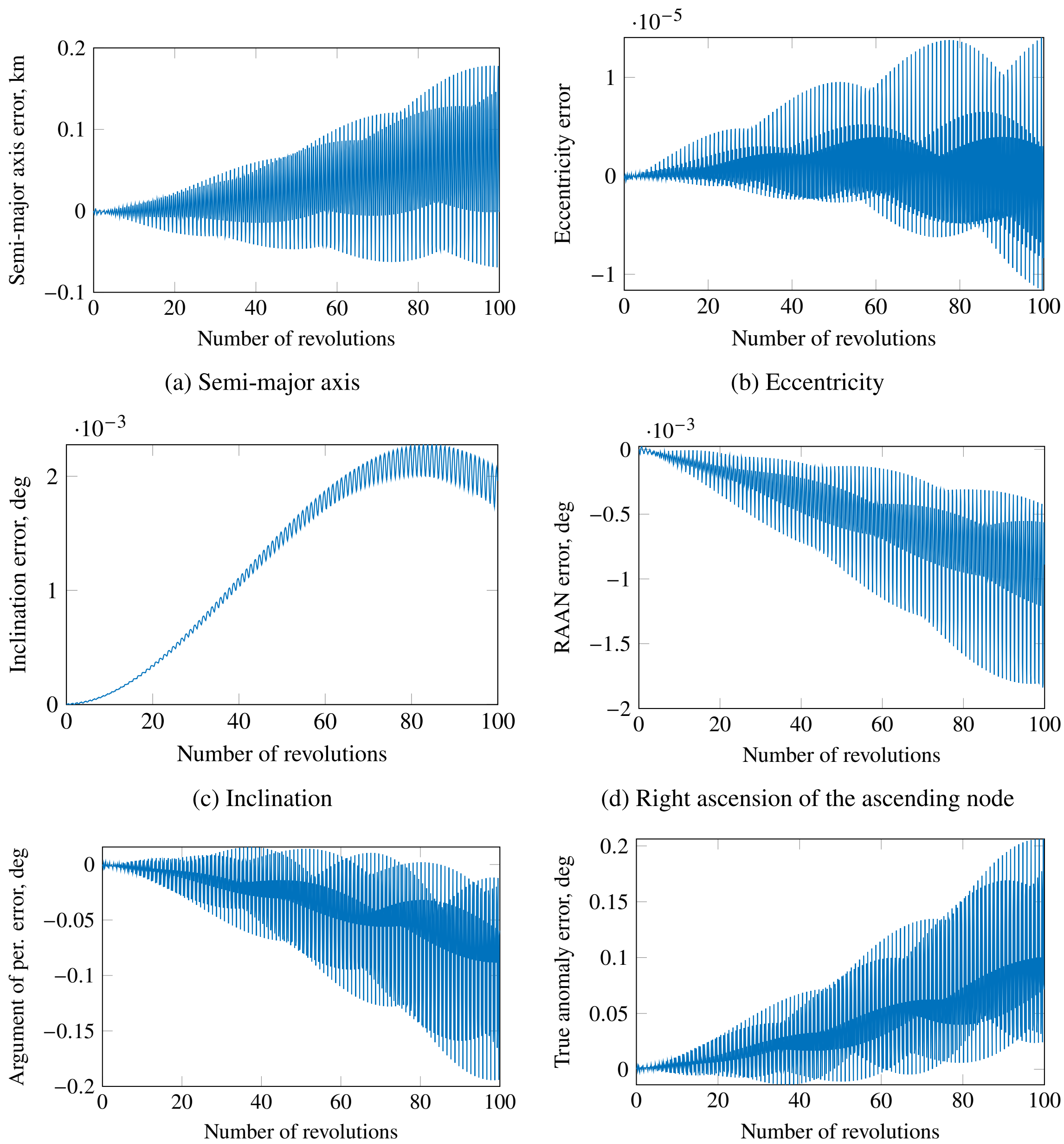

(a) Semi-major axis

(b) Eccentricity

(c) Inclination

(d) Right ascension of the ascending node

(e) Argument of periapsis

(f) True anomaly

Figure 7: Propagation error obtained with EDMD and 6th order basis functions when considering J_2 and atmospheric drag.

Combination of J_2 and Atmospheric Drag

For the combination of J_2 and atmospheric drag, we select an orbit with the following initial conditions: initial semi-major axis of $6906\,\mathrm{km}$, eccentricity of 0.082, inclination of $36.3°$, right ascension of the ascending node (RAAN) of $25.1°$, argument of periapsis of $125.5°$, and true anomaly of $29.5°$. The training data for EDMD includes orbits with altitudes between 400 and $700\,\mathrm{km}$ and orbital elements around the reference orbit. The evolution of the error for each element obtained with EDMD and 6th order basis functions is shown in Fig. 7 for 100 revolutions. Although the error increases over time, EDMD captures the evolution of the orbital elements quite accurately, with a final position error below $1.5\,\mathrm{km}$.

CONCLUSION

This work presents a quadrature-based Extended Dynamic Mode Decomposition (qEDMD) approach within the Koopman operator framework. Through a thorough comparison with standard EDMD and the analytical Galerkin method, we demonstrate that qEDMD significantly improves the convergence rate of the Koopman operator. This enhancement is crucial for onboard predictions where rapid and precise computations are required. To make this approach more practical, we incorporate atmospheric drag into the Koopman operator method. Our results show that it is feasible to accurately predict the state of a spacecraft affected by both J_2 perturbation and drag over multiple orbital revolutions. Future work will improve the numerical conditioning of the Koopman matrices and consider higher-order basis functions to further enhance accuracy.

ACKNOWLEDGMENTS

This work was funded under the Air Force Office of Scientific Research (AFOSR) Space University Research Initiative grant (FA95502210092).

REFERENCES

[1] S. L. Brunton, M. Budišić, E. Kaiser, and J. N. Kutz, “Modern Koopman Theory for Dynamical Systems,” *SIAM Review*, Vol. 64, No. 2, 2022, pp. 229–340, 10.1137/21M1401243.

[2] M. Budišić, R. Mohr, and I. Mezić, “Applied Koopmanism,” *Chaos: An Interdisciplinary Journal of Nonlinear Science*, Vol. 22, No. 4, 2012, p. 047510, 10.1063/1.4772195.

[3] S. E. Otto and C. W. Rowley, “Koopman Operators for Estimation and Control of Dynamical Systems,” *Annual Review of Control, Robotics, and Autonomous Systems*, Vol. 4, No. 1, 2021, pp. 59–87, 10.1146/annurev-control-071020-010108.

[4] M. L. Castaño, A. Hess, G. Mamakoukas, T. Gao, T. Murphey, and X. Tan, “Control-Oriented Modeling of Soft Robotic Swimmer with Koopman Operators,” *2020 IEEE/ASME International Conference on Advanced Intelligent Mechatronics (AIM)*, 2020, pp. 1679–1685, 10.1109/AIM43001.2020.9159033.

[5] D. Arnas and R. Linares, “Approximate Analytical Solution to the Zonal Harmonics Problem Using Koopman Operator Theory,” *Journal of Guidance, Control, and Dynamics*, Vol. 44, No. 11, 2021, pp. 1909–1923, 10.2514/1.G005864.

[6] T. Chen and J. Shan, “Koopman-Operator-Based Attitude Dynamics and Control on SO(3),” *Journal of Guidance, Control, and Dynamics*, Vol. 43, No. 11, 2020, pp. 2112–2126, 10.2514/1.G005006.

[7] S. Servadio, W. Parker, and R. Linares, “Uncertainty Propagation and Filtering via the Koopman Operator in Astrodynamics,” *Journal of Spacecraft and Rockets*, Vol. 60, No. 5, 2023, pp. 1639–1655, 10.2514/1.A35688.

[8] E. L. Jenson, M. Bando, K. Sato, and D. J. Scheeres, “Robust Nonlinear Optimal Control Using Koopman Operator Theory,” *2022 AAS/AIAA Astrodynamics Specialist Conference*, 2022. Paper AAS 22-647.

[9] R. Power and K. Howell, “Numerical Methodology for Extending Koopman Operator Theory Application in the CRTBP,” *AAS/AIAA Astrodynamics Specialist Conference*, 2023.

[10] J. Ng and H. H. Asada, "Data-Driven Encoding: A New Numerical Method for Computation of the Koopman Operator," *IEEE Robotics and Automation Letters*, Vol. 8, No. 7, 2023, pp. 3940–3947, 10.1109/LRA.2023.3273515.

[11] K. Zheng, P. Huang, and G. P. Fettweis, "Optimal Control of Quadrotor Attitude System Using Data-driven Approximation of Koopman Operator," *IFAC-PapersOnLine*, Vol. 56, No. 2, 2023, pp. 834–840. 22nd IFAC World Congress, 10.1016/j.ifacol.2023.10.1669.

[12] M. J. Colbrook, Q. Li, R. V. Raut, and A. Townsend, "Beyond expectations: residual dynamic mode decomposition and variance for stochastic dynamical systems," *Nonlinear Dynamics*, Vol. 112, Dec 2023, p. 2037–2061, 10.1007/s11071-023-09135-w.

[13] C. Hofmann, S. Servadio, R. Linares, and F. Topputo, "Advances in Koopman Operator Theory for Optimal Control Problems in Space Flight," *AAS/AIAA Astrodynamics Specialist Conference*, 8 2022. Paper AAS 22-759.

[14] M. O. Williams, I. G. Kevrekidis, and C. W. Rowley, "A Data–Driven Approximation of the Koopman Operator: Extending Dynamic Mode Decomposition," *Journal of Nonlinear Science*, Vol. 25, No. 6, 2015, pp. 1307–1346, 10.1007/s00332-015-9258-5.

[15] F. Heiss and V. Winschel, "Likelihood Approximation by Numerical Integration on Sparse Grids," *Journal of Econometrics*, Vol. 144, No. 1, 2008, pp. 62–80, 10.1016/j.jeconom.2007.12.004.

[16] D. Arnas, "Solving Perturbed Dynamic Systems Using Schur Decomposition," *Journal of Guidance, Control, and Dynamics*, Vol. 45, No. 12, 2022, pp. 2211–2228, 10.2514/1.G006726.